ACS Catalysis

Research Article

pubs.acs.org/acscatalysis

Tuning Catalytic Performance through a Single or Sequential Post-Synthesis Reaction(s) in a Gas Phase

Junjun Shan,[†,§] Shiran Zhang,[†,§] Tej Choksi,[‡] Luan Nguyen,[†,§] Cecile S. Bonifacio,[∥] Yuanyuan Li,[¶] Wei Zhu,[†,§,⊥] Yu Tang,[†,§] Yawen Zhang,[⊥] Judith C. Yang,[∥] Jeffrey Greeley,[‡] Anatoly I. Frenkel,*[,¶] and Franklin Tao*[,†,§]

[†]Department of Chemical and Petroleum Engineering, University of Kansas, Lawrence, Kansas 66045, United States

[§]Department of Chemistry, University of Kansas, Lawrence, Kansas 66045, United States

[‡]Department of Chemical Engineering, Purdue University, West Lafayette, Indiana 47907, United States

[∥]Department of Chemical and Petroleum Engineering, University of Pittsburgh, Pittsburgh, Pennsylvania 15261, United States

[⊥]College of Chemistry, Peking University, Beijing 10080, China

[¶]Department of Physics, Yeshiva University, New York, New York 10016, United States

Supporting Information

ABSTRACT: Catalytic performance of a bimetallic catalyst is determined by geometric structure and electronic state of the surface or even the near-surface region of the catalyst. Here we report that single and sequential postsynthesis reactions of an as-synthesized bimetallic nanoparticle catalyst in one or more gas phases can tailor surface chemistry and structure of the catalyst in a gas phase, by which catalytic performance of this bimetallic catalyst can be tuned. Pt−Cu regular nanocube (Pt−Cu RNC) and concave nanocube (Pt−Cu CNC) are chosen as models of bimetallic catalysts. Surface chemistry and catalyst structure under different reaction conditions and during catalysis were explored in gas phase of one or two reactants with ambient-pressure X-ray photoelectron spectroscopy (AP-XPS) and extended X-ray absorption fine structure (EXAFS) spectroscopy. The newly formed surface structures of Pt−Cu RNC and Pt−Cu CNC catalysts strongly depend on the reactive gas(es) used in the postsynthesis reaction(s). A reaction of Pt−Cu RNC-as synthesized with H_2 at 200 °C generates a near-surface alloy consisting of a Pt skin layer, a Cu-rich subsurface, and a Pt-rich deep layer. This near-surface alloy of Pt−Cu RNC-as synthesized-H_2 exhibits a much higher catalytic activity in CO oxidation in terms of a low activation barrier of 39 ± 4 kJ/mol in contrast to 128 ± 7 kJ/mol of Pt−Cu RNC-as synthesized. Here the significant decrease of activation barrier demonstrates a method to tune catalytic performances of as-synthesized bimetallic catalysts. A further reaction of Pt−Cu RNC-as synthesized-H_2 with CO forms a Pt−Cu alloy surface, which exhibits quite different catalytic performance in CO oxidation. It suggests the capability of generating a different surface by using another gas. The capability of tuning surface chemistry and structure of bimetallic catalysts was also demonstrated in restructuring of Pt−Cu CNC-as synthesized.

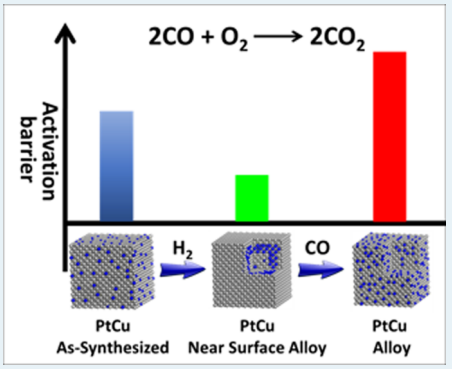

KEYWORDS: *bimetallic, ambient pressure X-ray photoelectron spectroscopy, restructuring, CO oxidation, tuning, synthesis*

1. INTRODUCTION

It is generally accepted that the structure and composition of the surface or the near-surface region of a bimetallic catalyst are the crucial factors determining its catalytic performance. As reported in the literature,[1] a slight difference in surface composition or atomic fraction of the surface or the subsurface of a single-crystal model catalyst by a few percent of second metal atoms could cause a distinctly different catalytic performance. For example, 3% of Au atoms deposited on surface of Ni(111) significantly change catalytic performance of Ni(111) in steam reforming.[1] In addition, a slight variation of surface composition of Pd(111) by doping different Au atoms up to a few percent can significantly increase catalytic activity of acetoxylation of ethylene to vinyl acetate on Pd(111).[2]

In some cases, surface composition of a bimetallic nanoparticle could be tuned through changing its bulk composition because the latter can be readily changed through synthesis.[3−6] However, it is extremely challenging to establish a correlation between surface and bulk compositions during synthesis in solution. Thus, it is challenging to predictively tune surface composition and structure through changing bulk composition and structure. This challenge results from the lack of in situ tracking of surface composition and identification of surface structures of nanoparticles in liquid state during nucleation and

Received: July 21, 2016
Revised: October 25, 2016
Published: October 28, 2016

DOI: 10.1021/acscatal.6b02054
ACS Catal. 2017, 7, 191−204

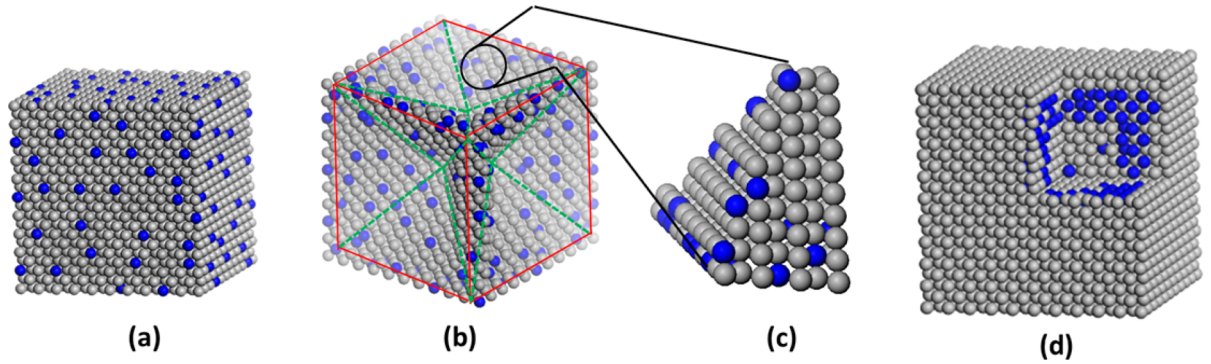

Figure 1. Structural models of (a) the as-synthesized Pt−Cu regular nanocube (Pt−Cu RNC), (b) the as-synthesized Pt−Cu concave nanocube (Pt−Cu CNC), (c) the stepped surface of Pt−Cu CNC, and (d) Pt−Cu near surface alloy (or called subsurface alloy) formed through a postsynthesis reaction in H_2 at 200 °C for Pt−Cu RNC. Note: the locations of blue and gray spots of these structural models only schematically show positions of Cu and Pt atoms on the surface of these nanocube catalysts.

growth of bimetallic nanoparticles in solution. The lack of in situ characterization techniques to track surface and near-surface regions of bimetallic particles during synthesis in solution, in turn, significantly limits the capability of tuning catalytic performances of bimetallic nanoparticle catalysts through the solution-based synthesis.

Tuning of chemistry and structure of surface of an as-synthesized catalyst through a postsynthesis reaction in a *gas* phase would be a straightforward approach to tune catalytic performance of a bimetallic catalyst because its *surface composition* in a gas phase can be readily measured with ambient-pressure X-ray photoelectron spectroscopy (AP-XPS). This approach is termed "post-synthesis reaction in a gas phase". Compared to the approach of tuning composition through synthesis in solution, the approach of "post-synthesis reaction in a gas phase" has two advantages. First, there do exist techniques for analyzing surfaces of bimetallic nanoparticles in a gas phase.[7−9] For example, surface chemistry (composition, oxidation state, electron transfer) of a bimetallic catalyst during annealing in gas phase, or during catalysis in a mixture of all reactant gases in a catalytic reaction, can be readily measured and tracked with ambient pressure X-ray photoelectron spectroscopy (AP-XPS).[9,10] Second, the surface free energy of constituent elements and chemisorption of reactive molecules in a gas phase could drive metal atoms of one element to segregate to the surface or migrate to the inner part of a bimetallic nanoparticle[8,11−15] and thus modify the catalyst structure. *We assumed that a potential restructuring of bimetallic nanoparticles could be used to develop a new catalyst. Here Pt−Cu bimetallic nanoparticles were chosen to study to test whether a potential restructuring of a catalyst surface could be used to develop a new catalyst.*

DFT calculations reported that adsorption energy of CO on Pt atoms of a single-crystal model catalyst consisting of Pt surface layer and Cu-rich subsurface, called near-surface alloy (NSA), is markedly lower than that of pure Pt surface.[16] It indicates that a Pt nanocube with a subsurface layer of Cu atoms (Figure 1d) could exhibit a high activity for CO oxidation compared to a pure Pt nanocube. However, it is quite challenging to synthesize such a near surface alloy through a wet chemistry method in solution, although Pt−Cu random alloy nanocubes can be synthesized in solution. Because of the challenge in synthesis of Pt−Cu NSA in solution, the possibility of preparation of a Pt−Cu NSA through a postsynthesis reaction of Pt−Cu regular nanocube (Pt−Cu RNC) in a gas phase was considered. If successful, it would test whether a postsynthesis reaction in a gas phase could prepare a Pt−Cu NSA and how catalytic performance of as-synthesized bimetallic nanoparticles can be tuned through a postsynthesis reaction in a reactive gas such as H_2 (Figure 2a) or two sequential reactions in two different reactive gases such as H_2 with a following CO (Figure 2c).

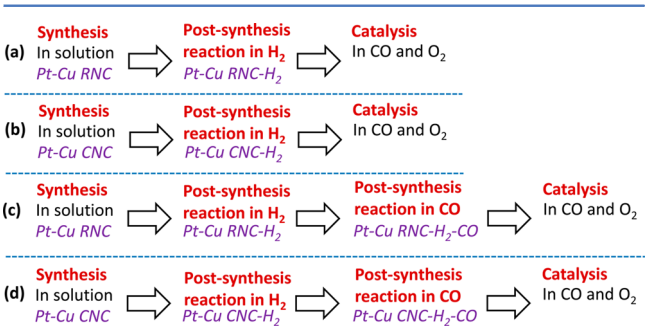

Figure 2. Procedures to form a new catalyst surface through a single or sequential reaction in a gas phase.

Other than Pt−Cu RNC, the selection of Pt−Cu concave nanocube (Pt−Cu CNC) (Figure 1b) is driven by the hypothesis that the under-coordinated step sites of a stepped surface (Figure 1c) could play a distinctly different role in formation of a new catalyst structure through a postsynthesis reaction in a gas phase. As under-coordinated metal sites widely exist in industrial metal catalysts and play a vital role in many catalytic reactions, a parallel study of Pt−Cu CNC with exposed stepped surfaces is expected to provide insights on the role of step sites in the capability of tuning catalytic performance through a postsynthesis reaction in a gas phase. Thus, both Pt−Cu RNC and Pt−Cu CNC were synthesized in solutions. As the mismatch of lattices of Pt and Cu increases along the increase of concentration of Cu in the Pt−Cu bimetallic nanocubes, we tended to choose a relatively low composition of Cu. On the other hand, the migration and segregation effect of Cu could be unmeasurable if the concentration of Cu is too low. Thus, Pt−Cu RNC and Pt−Cu CNC with a bulk concentration of Cu of 20% were chosen in this work.

H_2 and CO were chosen as reactant gases to test whether catalytic activity and selectivity can be tuned. Surface chemistry of Pt−Cu RNC and Pt−Cu CNC (1) in H_2 (termed Pt−Cu

DOI: 10.1021/acscatal.6b02054
ACS Catal. 2017, 7, 191−204

RNC-H_2 or Pt−Cu CNC-H_2), (2) during CO oxidation after a postsynthesis reaction in H_2, (3) in CO after a postsynthesis reaction in H_2 (termed Pt−Cu RNC-H_2−CO or Pt−Cu CNC-H_2−CO), or (4) during CO oxidation on Pt−Cu RNC-H_2−CO or Pt−Cu CNC-H_2−CO, were studied with AP-XPS in this work. Distribution of elements from the topmost surfaces to the cores of these generated nanoparticle catalysts were examined with high-angle annular dark-field scanning transmission electron microscopy (HAADF-STEM). Particularly, line scans of energy-dispersive X-ray (EDX) spectroscopy in HAADF-STEM can provide insights on the geometric distribution of Pt and Cu atoms of Pt−Cu RNC-as synthesized and Pt−Cu CNC-as synthesized and those experiencing different postsynthesis reaction(s) in gas phase(s). Coordination environments of both Pt and Cu atoms of these catalysts under reaction conditions and during catalysis were studied with in situ EXAFS. Segregation energies of metal atoms of Pt−Cu RNC and Pt−Cu CNC covered with adsorbates were calculated with periodic density function theory (DFT). Kinetics studies of CO oxidation on these catalysts were performed in a fixed-bed flow reactor. Their activation energies were calculated through Arrhenius plots obtained from kinetics studies. Details of kinetics studies of these catalysts were described in experimental sections and Supporting Information.

Reaction at 200 °C with H_2 for Pt−Cu RNC-as synthesized forms a Cu-rich subsurface in Pt−Cu RNC-H_2 which exhibits an activation barrier of 39 ± 4 kJ/mol for CO oxidation, largely lower than that of the Pt−Cu RNC-as synthesized (128 ± 7 kJ/mol). Catalyst Pt−Cu RNC-H_2−CO formed through a treatment in H_2 first and then CO gives an activation barrier of 173 ± 11 kJ/mol, which is significantly higher than that of Pt−Cu RNC-as synthesized. The extent of restructuring depends on the original surface structure of the bimetallic nanoparticle. For example, compared to the significant decrease of activation barrier of Pt−Cu RNC-as synthesized after annealing at 200 °C in H_2, the annealing of the Pt−Cu CNC-as synthesized only slightly changes its catalytic performance. Overall, our studies of this work illustrate that a change of chemistry and structure of surface or near surface region of a catalyst driven by a postsynthesis reaction in a gas phase can significantly tune its catalytic activity. It demonstrated the capability of significantly tuning catalytic performance through one or more reactions in a gas phase after synthesis.

2. EXPERIMENTAL DETAILS AND METHOD OF DFT CALCULATIONS

2.1. Synthesis of Pt−Cu RNC Bimetallic Nanocubes. Pt−Cu regular nanocubes were prepared under hydrothermal conditions. A coreduction of Pt(II) and Cu(II) species in aqueous solution with the selective adsorption behavior of Br^- ions formed 7.8 nm Pt−Cu RNC. KBr (9 mmol) and 100 mg of polyvinylprrolidone (PVP) were first dissolved in water. 0.03 mmol of K_2PtCl_4, 0.03 mmol of $CuCl_2$ and 0.15 mmol of HCl aqueous solution were added with stirring. The solution was diluted to 15 mL by water and transferred into a 25 mL Teflon-lined stainless steel autoclave. The autoclave was sealed and kept at 160 °C for 4 h. After it cooled down to room temperature, a black colloidal solution was obtained. Pt−Cu RNC was acquired by centrifuging the mixture of as-prepared solution with 45 mL of acetone. The black precipitates were washed by ethanol/acetone and water/acetone for several times. Finally, the Pt−Cu RNC was dissolved in water and kept for the further characterization.

2.2. Synthesis of Pt−Cu CNC Bimetallic Nanocubes. Pt−Cu CNC nanocubes (11.7 nm) were synthesized through progressive galvanic replacement induced by H^+, Cu^{2+}, and Br^-. The synthetic method and post-treatment procedure of Pt−Cu CNC were the same as those of Pt−Cu RNC, except that 0.6 mmol HCl was added in the synthesis of Pt−Cu CNCs, instead of the 0.15 mmol HCl in the synthesis of Pt−Cu RNC.

2.3. TEM Characterization. Transmission electron microscopy (TEM), high-resolution transmission electron microscopy (HRTEM), and energy-dispersive X-ray spectroscopy (EDX) were conducted on a FEI TITAN 80−300 TEM operated at 300 kV with an Oxford EDXS attachment. The Pt−Cu RNC and Pt−Cu CNC samples for TEM characterization were prepared by dropping their colloidal solution onto carbon-supported nickel grids. Samples for EDX characterization were conducted with a molybdenum specimen holder to eliminate copper signals from the specimen holder. The high-resolution transmission electron microscopy (HRTEM) image illustrated that Pt−Cu RNC were bounded with six {100} facets. The contrast of TEM images of Pt−Cu CNC confirmed the concave surface for the nanocubes. As illustrated in Figure 1c, the angle between the concave surface and the (100) surface was not 45°. It demonstrated that the exposed surface should be high Miller index facets, not {100} planes. HAADF-STEM technique was used to study the distribution of Pt and Cu atoms of Pt−Cu nanoparticles. It is noted that HAADF-STEM is not an average technique. It provides information on single nanoparticles. EDX line scan of single nanoparticles was used to provide information on the distribution of elements at different locations of a single nanoparticle. Due to the least sampling volume of a single nanoparticle in the line scan of EDX, the signal-to-noise ratio is low, and thus, the base lines are fluctuating as shown in the spectra of line scan of EDX in HAADF-STEM. The fluctuations of the base lines due to the nature of this technique do not suggest the change of the distributions of Pt and Cu. Compared to imaging and line scan of EDX of HAADF-STEM, AP-XPS and EXAFS provide average information on a large number of nanoparticles.

2.4. Measurements of Catalytic Performance and Kinetics Studies. For kinetic studies, catalyst samples for measurements of catalytic performance were prepared with the following two methods. Method no. 1 was used in the preparation of samples for kinetics studies shown in Figure 4. In Method no. 1, the preparation of each sample includes two steps. Step 1: the diluted solution of Pt−Cu RNC-as synthesized or Pt−Cu CNC-as synthesized dispersed in ethanol was deposited onto silica nanoparticles (40−60 nm) via incipient wetness impregnation for several times; the final mass ratio of Pt−Cu nanoparticles to silica particles is about 5%; ethanol was evaporated at 50 °C; a subsequent heating to 120 °C in vacuum oven was performed to remove the left ethanol; step 2: weigh 5 mg of catalyst sample (metal nanoparticles impregnated on silica particles) to mix with sand (50−70 mesh, Aldrich), which was purified with aqua regia. After the Pt−Cu RNC/SiO_2 or Pt−Cu CNC/SiO_2 was well-mixed with the purified sand, the sample was loaded to a quartz tube for measurements of catalytic performance.

Method no. 2 was used in preparation of samples for kinetics studies shown in Figures S1−S7. In Method no. 2, catalyst samples were prepared by directly diluting Pt−Cu RNC or Pt−Cu CNC nanoparticles with porous silica (30−60 mesh, Aldrich) through incipient wetness impregnation. The ethanol solution of Pt−Cu RNC-as synthesized or Pt−Cu CNC-as synthesized was dropped into porous silica with vigorous agitation until the porous silica was wetted. The wet silica was heated in an oven at 50 °C to evaporate ethanol. The process was repeated for several times until the calculated amount (~5 wt %, mass ratio of Pt−Cu nanoparticles to the total mass of Pt−Cu nanoparticles and silica particles) of Pt−Cu RNC or Pt−Cu CNC was reached. A following drying in vacuum oven at 120 °C thoroughly evaporated surface remaining ethanol. The diluted catalyst (Pt−Cu RNC/SiO_2 or Pt−Cu CNC/SiO_2) was loaded to a quartz reactor for a reaction in a gas phase and a following measurement of catalytic performances.

Three types of quartz tubes with a different internal diameter of 1/4″, 3/16″, or 1/8″ were used to load a catalyst. A K-type thermocouple installed on an ultratorr adapter for good sealing was inserted to a fixed-bed flow reactor. Its end is located at the center of the catalyst bed. Measurements of the catalytic activity of these catalysts for CO

DOI: 10.1021/acscatal.6b02054
ACS Catal. 2017, 7, 191−204

oxidation were carried out at atmospheric pressure in the reactor. Two series of parallel catalytic measurements were done. One is the catalysis studies by varying the internal diameter of the quartz tubes; the other is the catalysis studies by varying the amount of loaded catalyst; the purpose of the two series of parallel studies is to justify the eligibility of kinetics studies reported in this work. Catalysts were pretreated in H_2, or H_2 and then CO at a certain temperature as described in the main text or marked in figures and tables. Upon the pretreatment (reactant in gas phase at certain temperature), catalyst was cooled to room temperature; gases of pretreatment were switched to a mixture of 4 mL/min pure CO, 10 mL/min pure O_2 balanced with 36 mL/min Ar for CO oxidation. The catalyst was heated in a furnace equipped with a proportional-integral-derivative (PID) temperature controller (Omega). The gas composition of the mixture of reactants is 8% CO, 20% O_2, and 72% Ar. Flow rates of these gases were controlled with three mass flow meters/controllers (Dakota Instruments, Inc.). The effluent gas of the downstream of the reactor was connected to a gas chromatograph (8610C, SRI Instruments) equipped with a HayeSep D (6′ × 1/8″) packed column, a molecular sieve 13× (6′ × 1/8″) packed column, and a thermal conductivity detector (TCD) for the analysis of both the reactants and products. In kinetics studies of CO oxidation on Pt−Cu catalysts, conversion rates of CO were controlled at ≤15% to meet the kinetics controlled regime. Activation energies of the newly formed catalytic surfaces in CO oxidation were calculated through Arrhenius plot of ln $[X]$ (X: conversion) as a function of $1000/T$ (T: temperature in Kevin).

The reliability of catalysis tests with this fix-bed reactor was checked through a blank experiment with the same experimental parameters including reactant gases, flow rate, and reaction temperature. In the blank experiment, only silica supporting material was loaded. Before each kinetics study a blank experiment was always performed. There was no CO_2 formed in all blank experiments.

2.5. In Situ Studies Using Ambient Pressure X-ray Photoelectron Spectroscopy. In situ studies of surface chemistry of Pt−Cu RNCs and CNCs were performed on the home-built ambient pressure XPS using monochromated Al Kα in the Tao group.[18,19] In terms of the resolution of this system, the measured full width at half-maximum (fwhm) of the Ag $3d_{5/2}$ spectrum of Ag thin film is 0.3 eV.[18,19] Binding energies of Au and Ag samples were calibrated to Au $4f_{7/2}$ at 84.0 eV and Ag $3d_{5/2}$ at 368.3 eV.[20] A sample was inserted and located at the cross point of Rowland circle of the monochromator and the aperture of the differentially pumped energy analyzer. The distance between sample surface and the aperture of prelens of the differential pumping stage remains at 0.3−0.5 mm, which is shorter than the mean free paths of photoelectrons traveling in a gaseous environment of 5 Torr.

The surface composition of Pt−Cu nanoparticles formed through restructuring (such as H_2 at 200 °C or H_2 at 200 °C with a following step in CO at 350 °C) is the stable composition of a surface over the time scale of the experiments. The XPS spectra at each of these conditions were collected cyclic. "Cyclic" means that the XPS data were collected cycle by cycle. In each cycle, both Cu 2p and Pt 4f were collected. With a cyclic collection mode, we can readily judge whether there is a change of surface composition as a function of time. Lack of a change of surface composition as a function of time suggests that the surface composition is stable before data acquisition. Each cycle took a few to 10 min. We collected data with 10−20 cycles for better signal/noise ratio. In this way, any potential time-dependent change of surface composition can be identified. In all the data acquisition of cyclic mode of this work, we did not observe time-dependent change of surface composition; it suggests that the surface composition was stable before data acquisition.

2.6. X-ray Absorption near Edge Structure and Extended X-ray Absorption Fine Structure. In situ X-ray absorption spectroscopy measurements were performed at the Beamline 2−2 at the Stanford Synchrotron Radiation Lightsource at SLAC National Accelerator Laboratory. A double-crystal Si (220) monochromator was used to collect X-ray absorption spectroscopy data for Cu K-edge and Pt L_3-edge. Sample powders were loaded to a Clausen Cell,[21,22] using Kapton tube (3 mm o.o.), which can be heated up to 350 °C. Pt L_3 edge spectra were collected in transmission mode and Cu K edge spectra were collected in fluorescence mode using Ge detector. The beam size was 0.5 mm vertically and 4 mm horizontally. X-ray absorption coefficients of metal Cu and Pt foils were measured in reference mode for X-ray energy calibration and data alignment. Up to four consecutive scans were collected at each stage of the reaction to improve the signal-to-noise ratio. The detailed regimes for sample treatments and data collections were the following: (1) collecting Cu K-edge and Pt L_3-edge in ambient conditions; (2) treating sample at a certain temperature in 5%H_2/He mixture for 3 h; (3) cooling to room temperature, while keeping the flow of 5% H_2/He mixture, and collect Cu and Pt edge data; (4) stopping the H_2 flow and introducing 10% CO/He, followed by annealing to a certain temperature in CO; (5) decreasing the temperature to room temperature and collecting Cu and Pt edge data; (6) flowing 8%CO + 20%O_2 + 72%He mixture while increasing temperature to 200 °C; (7) decreasing temperature to room temperature, followed by collecting Cu and Pt edge data.

The data in the XANES region of the absorption coefficient were examined by applying the same procedure for pre-edge line fitting, postedge curve fitting, and edge-step normalization to all data. XANES and EXAFS data processing and analysis were performed using the IFEFFIT package.[23] EXAFS data modeling and analysis were performed using standard procedures.[24−28] The passive electron reduction factors (also known as EXAFS amplitude factors) were obtained to be 0.84 ± 0.03 from the fit to the Pt foil data and 0.79 ± 0.04 from the fit to the Cu foil data. They were subsequently fixed to be 0.84 and 0.79 for the Pt and Cu absorption edge data analyses, respectively, in the analysis of all Cu−Pt catalysts. For Cu edge, the fitting k range is 2.0−8.3 Å^{-1} and the fitting R range is 1.6−3.1 Å. For Pt edge, the fitting k range is 2.8−15.5 Å^{-1} and the fitting R range is 1.7−3.2 Å. The model used for fitting Cu edge spectra includes Cu−Cu and Cu−Pt bonds, and for the fitting Pt edge spectra, the model includes Pt−Pt and Pt−Cu bonds. To improve the uncertainties of fitting results and break the correlation between the coordination numbers (N) and the disorder factors (σ^2), the Cu and Pt edge spectra under all conditions for each catalyst were fitted simultaneously. The constrains applied were the following: (1) $R_{Cu-Pt} = R_{Pt-Cu}$, (2) $\sigma^2_{Cu-Pt} = \sigma^2_{Pt-Cu}$, (3) the shifts of the threshold energy (ΔE) were constrained to be the same for all Pt (and, separately, Cu) edge data, and (4) σ^2 values were constrained to be the same for all Cu−Cu (and, separately, Pt−Pt) contributions.

2.7. Periodic Density Functional Theory Calculations. Periodic density functional theory (DFT) calculations were performed with GPAW, a real-space, grid-based DFT code, developed by Mortensen and co-workers,[29,30] through the "ASE" package,[17] that employs the projector augmented wave method to treat core electrons.[31,32] A grid spacing of 0.16 Å was employed, and all calculations were carried out with the PBE functional,[33] for which a Pt lattice constant of 3.996 Å was determined. A Fermi temperature of 0.1 eV was employed to accelerate numerical convergence. For calculations on the PtCu(100) surface, a $p(2\sqrt{2}\ x2\sqrt{2})R45°$ unit cell with five metal layers and eight metal atoms per layer was employed, of which the top three layers were allowed to relax completely with a force termination criterion of 0.05 eV/Å per atom. For the PtCu(310) surface, a similar arrangement of five metal layers perpendicular to the terrace planes, with six metal atoms per layer, was employed, and the top three layers were again allowed to relax completely. Further details about positions of Cu atoms within the supercell for both surfaces can be found in the Supporting Information. Vacuum regions of 12 Å were included in all calculations on all surfaces. Dipole corrections were applied to eliminate spurious dipole−dipole interactions between metal slabs. Enthalpic contributions to the segregation energies were calculated as the difference in energy between a slab with Pt/Cu switches and the reference slab. Changes in entropy (configurational) during the segregation process, which were around the order of 1 kT (~0.02 eV at 473 K), were not included in the segregation energy. Consistent with prior studies,[34] the enthalpic barrier for segregation has been used to understand trends in segregation processes. We further point out that, because these and related studies have found that determination of segregation energies provides powerful insight

DOI: 10.1021/acscatal.6b02054
ACS Catal. 2017, 7, 191−204

into nanocatalyst structure and stability, it is not essential to determine a complete, step-by-step atomistic mechanism for the segregation process, and such an analysis would be beyond the scope of the present work. To ensure numerical accuracy, segregation energies were calculated with Monkhorst–Pack *k*-point grids ranging from (3, 3, 1) to (6, 6, 1). As the difference in segregation energy between (5, 5, 1) and (6, 6, 1) *k*-point grids was less than 5 meV/atom, a (5, 5, 1) grid was employed for both the (100) and (310) surfaces. Gas-phase energies for H_2 and CO at the gamma point were obtained using a 11 × 12 × 13 Å unit cell. Methodological details describing adsorption sites and ab initio phase diagrams are presented in the Supporting Information.

3. RESULTS AND DISCUSSION

3.1. Kinetics Studies of Pt–Cu RNC-Based and Pt–Cu CNC-Based Catalysts Formed through Postsynthesis Reactions in Gas Phase(s). Figure 3 presents TEM images of Pt–Cu RNC and Pt–Cu CNC synthesized through reduction of Pt and Cu precursors with a method described in the experimental details. Pt–Cu RNC-as synthesized and Pt–Cu CNC-as synthesized have sizes of 7.8 ± 1 nm and 11.7 ± 2 nm, respectively. Catalytic performances of CO oxidation on Pt–Cu RNC-as synthesized and Pt–Cu CNC-as synthesized and catalysts generated from one or sequential postsynthesis reactions in gas phase(s) including Pt–Cu RNC-H_2, Pt–Cu RNC-H_2–CO, Pt–Cu CNC-H_2 and Pt–Cu CNC-H_2–CO (Figure 2) were investigated in a kinetics controlled regime. The details of kinetics studies were described in the experimental section of the main text and the Supporting Information. Figure 4 and Figures S1–S4 present Arrhenius plots of kinetics studies of CO oxidation on Pt–Cu RNC-as synthesized, Pt–Cu RNC-H_2, Pt–Cu RNC-H_2–CO, Pt–Cu CNC-as synthesized, Pt–Cu CNC-H_2, and Pt–Cu CNC-H_2–CO. For comparison, kinetics studies of CO oxidation on pure Pt nanocubes pretreated in H_2 at 200 °C were performed under the same catalytic condition as that of other catalysts (Figure 4 and Figure S5). The catalytic activation barrier of CO oxidation on pure Pt nanocubes is ~92 ± 5 kJ/mol (entry 1 in Table 1). This is consistent with the activation energy of Pt catalysts reported in the literature.[34−36] Table 1 lists the activation energies of CO oxidation on Pt–Cu RNC and Pt–Cu CNC. Activation barriers for CO oxidation calculated from Arrhenius plots of these catalysts are 128 ± 7 kJ/mol for Pt–Cu RNC-as synthesized, 39 ± 4 kJ/mol for Pt–Cu RNC-H_2, 173 ± 11 kJ/mol for Pt–Cu RNC-H_2–CO, 109 ± 10 kJ/mol for Pt–Cu CNC-as synthesized, 72 ± 6 kJ/mol for Pt–Cu CNC-H_2, and 80 ± 8 kJ/mol for Pt–Cu CNC-H_2–CO. In addition, to validate these kinetics studies, the reaction orders of CO and O_2 of CO oxidation on Pt RNC-H_2 were measured with the same reactor as the kinetics studies of CO oxidation on Pt RNC-H_2. Our measurements showed that the reaction orders of O_2 and CO are 0.99 and −0.89, respectively (Figures S6 and S7), which are consistent with the literature.[23,24]

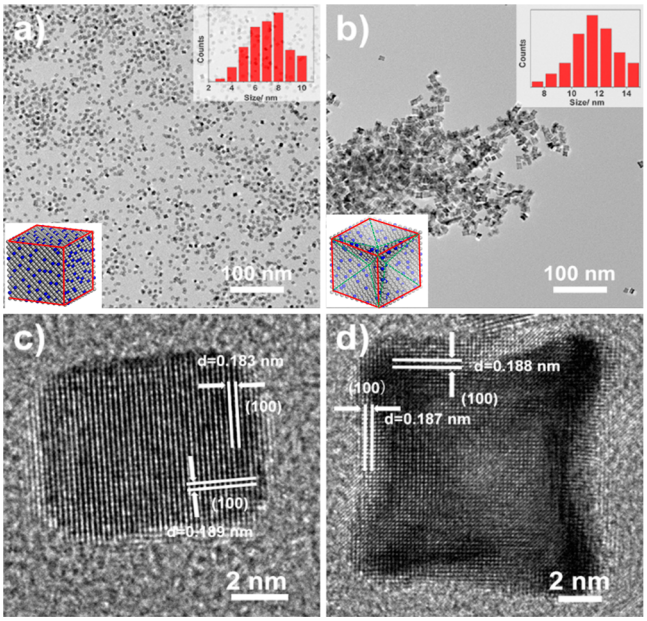

Figure 3. TEM images of Pt–Cu RNC-as synthesized and Pt–Cu CNC-as synthesized. (a) Large area of Pt–Cu RNC-as synthesized nanoparticles. (b) Large area of Pt–Cu CNC-as synthesized nanoparticles. (c) High-resolution TEM image of a Pt–Cu RNC-as synthesized nanoparticle. (d) High-resolution TEM image of a Pt–Cu CNC-as synthesized nanoparticle. Note: the locations of blue and gray spots of these insert structural models do not exactly present the positions of Cu and Pt atoms on surface of these nanocube catalysts.

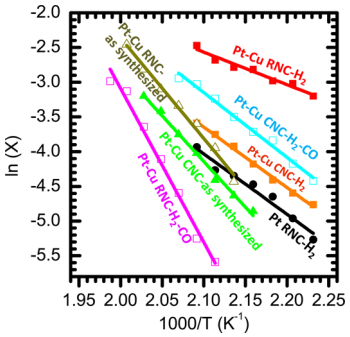

Figure 4. Arrhenius plots of CO oxidation on catalysts formed from pure Pt nanocubes, Pt–Cu RNC-as synthesized, and Pt–Cu CNC-as synthesized through a postsynthesis reaction in gas phase.

3.2. Structure of Pt–Cu RNC-H_2 Formed in a Postsynthesis Reaction in H_2 and Its Correlation to Catalytic Performance. *3.2.1. Change of Surface Composition Tracked with AP-XPS.* Surfaces of these catalysts were characterized with AP-XPS under a reaction condition (defined to characterization of a catalyst while it is in a gas environment of only *one reactant* of a catalytic reaction) or during catalysis (defined to characterization of a catalyst while it is in a gas environment of *all reactants* of a catalytic reaction). Both Pt 4f and Cu 2p peaks were collected. Their peak areas were integrated for calculations of surface compositions upon a calibration to their sensitivity factors. Peak positions of Pt 4f and Cu 2p were used to identify their oxidation states. All Pt 4f and Cu 2p spectra collected in this paper show that all Pt and Cu atoms of these catalysts as-synthesized and generated through one or sequential postsynthesis reactions (or called postsynthesis treatment) in gas phases are in metallic state as exampled in Figure S8. Figure 5a presents the evolution of atomic fractions of Pt and Cu on the Pt–Cu RNC-as synthesized during CO oxidation at different temperatures. It is noted that the locations of these blue and gray balls of these models in Figure 5 and all other figures (Figures 1, 3, 5, and 6) do not exactly present the actual positions of Cu and Pt atoms on surfaces of these catalysts. These models only schematically show the change of catalyst structure upon a different postsynthesis reaction in gas phase(s).

DOI: 10.1021/acscatal.6b02054
ACS Catal. 2017, 7, 191–204

Table 1. List of the Measured Activation Barriers of Different Catalysts

entry	catalysts	postsynthesis reaction(s)	activation energy (kJ/mol) in CO oxidation after postsynthesis reaction(s)
1	pure Pt RNC-H_2	H_2, 200 °C	92 ± 5
2	Pt−Cu RNC-as synthesized	N/A	128 ± 7
3	Pt−Cu RNC-H_2	H_2, 200 °C	39 ± 4
4	Pt−Cu RNC-H_2−CO	H_2 at 200 °C, CO at 350 °C	173 ± 11
5	Pt−Cu CNC-as synthesized	N/A	109 ± 10
6	Pt−Cu CNC-H_2	H_2, 200 °C	72 ± 6
7	Pt−Cu CNC-H_2−CO	H_2 at 200 °C, CO at 350 °C	80 ± 8

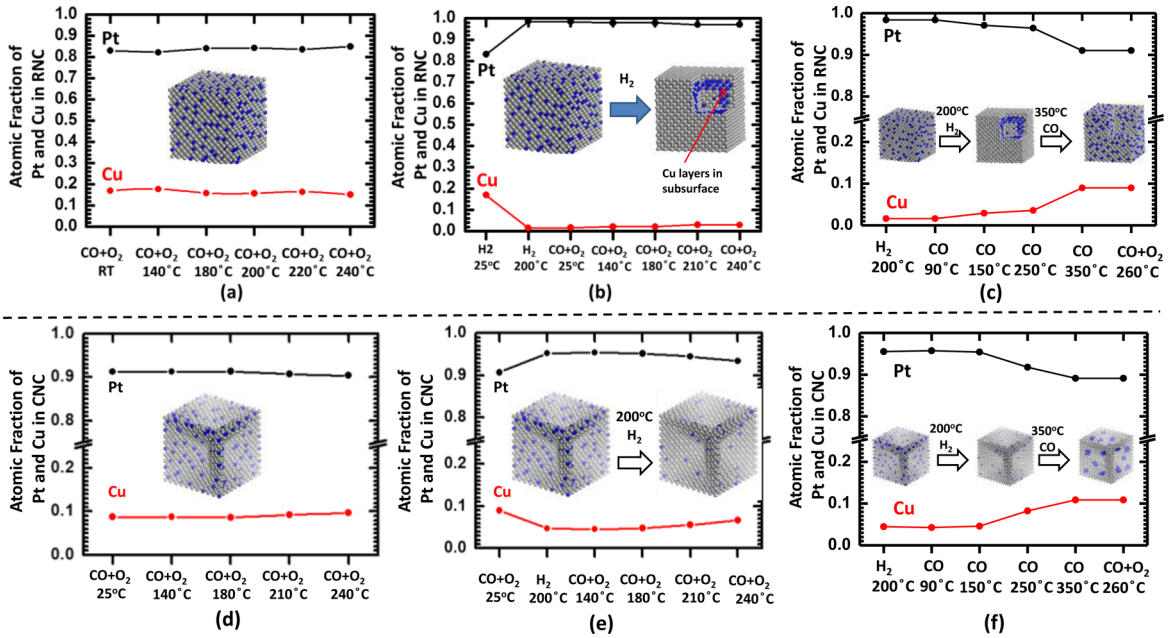

Figure 5. Evolution of surface composition (Pt and Cu atomic fractions) of Pt−Cu RNC-as synthesized or Pt−Cu CNC-as synthesized and those after postsynthesis reaction(s) in gas phase(s). (a) Pt−Cu RNC-as synthesized (without a reaction in H_2) in CO and O_2. (b) Pt−Cu RNC in H_2 at 200 °C and then CO oxidation. (c) Pt−Cu RNC in H_2 at 200 °C, CO up to 350 °C, and then in the mixture of CO and O_2. (d) Pt−Cu CNC-as synthesized (without a reaction in H_2) in CO and O_2. (e) Pt−Cu CNC in H_2 at 200 °C and then in CO and O_2. (f) Pt−Cu CNC in H_2 at 200 °C, in CO up to 350 °C, and then in the mixture of CO and O_2. Note: the locations of blue and gray spots of these structural schematics inserted to these figures do not represent the positions of Cu and Pt atoms on surface of these nanocube catalysts. The error bars of these measurements of atomic fractions are ±5% of the given atomic fractions.

In contrast to the high activation barrier of CO oxidation on the Pt−Cu RNC-as synthesized (128 ± 7 kJ/mol), surprisingly the activation energy of Pt−Cu RNC-H_2 is only 39 ± 4 kJ/mol (Figure 4 and entry 3 of Table 1). This quite low activation barrier suggests that the structure of Pt−Cu RNC-as synthesized was significantly changed upon reaction with H_2 at 200 °C (Pt−Cu RNC-H_2). Migration of Cu atoms to inner parts of the nanoparticles was confirmed through AP-XPS studies. As shown in Figure 5b, the postsynthesis reaction in H_2 at 200 °C has obviously decreased the concentration of Cu of the surface region of Pt−Cu RNC-as synthesized from 18% to 0−1%. Notably, the error bar of the measurement of the atomic fraction is ±5% of the measured atomic fraction (18%). Thus, the decrease of Cu concentration by 17% (18%−1%) is definitely larger than the error bar (18% × ± 5%= ± 0.5%).

3.2.2. Location of Cu Atoms in Surface Region of Pt−Cu RNC-H_2 Identified with EDX. The change of Cu concentration from 18% to 1% is significant, although the relative change in Pt concentration (from 82% to 99%) is only 21%. From the random alloy point of view, it seems that such change of concentration of Pt could not significantly change electronic state of the surface atoms and the corresponding catalytic performance. In fact, the postsynthesis reaction in H_2 results in a significant structural change of *surface region* of Pt−Cu RNC-as synthesized catalyst and thus an obvious change of electronic states of *Pt atoms of surface*. The observed decrease of surface composition of Cu from 18% to 0−1% upon the postsynthesis reaction in H_2 (Figure 5b) suggests that these Cu atoms in the surface layers migrated to an inner section of a nanocube; these migrated Cu atoms could locate at subsurface, deep layers, or even be homogeneously distributed in the whole region from subsurface to core. Unfortunately, AP-XPS cannot provide specific information on the new location of the migrated Cu atoms. Thus, EDX function of HAADF-STEM was used to identify the distribution of Pt and Cu atoms. A useful function of HAADF-STEM is the EDX spectroscopy line scan crossing a nanoparticle from an edge to its opposite side. It is noted that the fluctuation of the base lines of these EDX spectra in Figure 6 do not suggest a change of atomic fractions of Pt and Cu. As shown in Figure 6b1, EDX line scans of Cu Kα and Pt Lα of Pt−Cu RNC-H_2 revealed the sharp increase of Cu concentration (blue line in Figure 6b1) and simultaneously rapid decrease of Pt concentration (dark line) at subsurface which is about 0.5 nm below the outmost layer of the nanoparticle.

DOI: 10.1021/acscatal.6b02054
ACS Catal. 2017, 7, 191−204

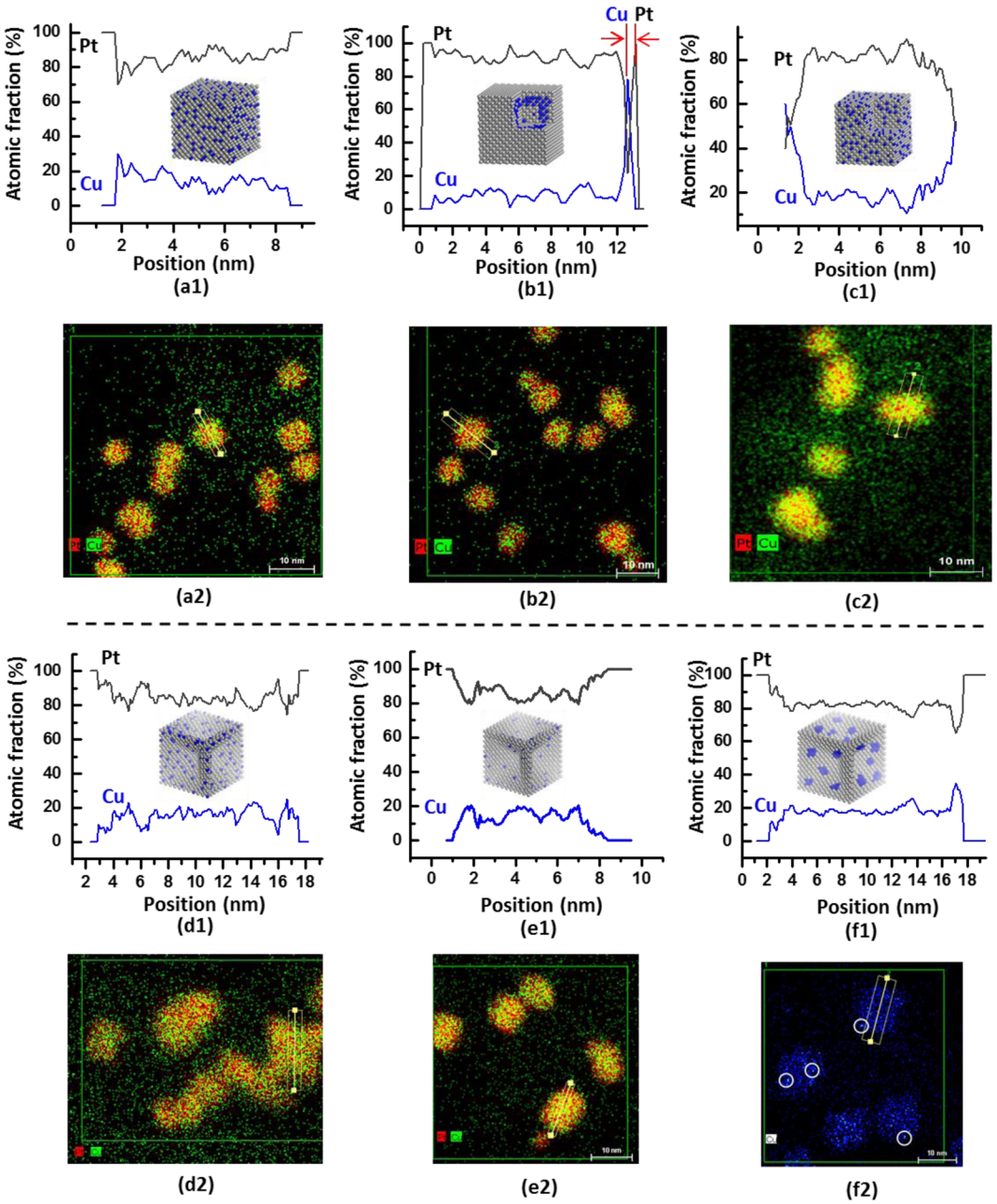

Figure 6. Energy-dispersive X-ray (Cu Kα and Pt Lα) spectra and mapping of Pt−Cu RNC-as synthesized nanoparticles and Pt−Cu CNC-as synthesized nanoparticles generated from them through postsynthesis reactions in gas phases. (a1 and a2) Pt−Cu RNC-as synthesized. (b1 and b2) Pt−Cu RNC-H_2. (c1 and c2) Pt−Cu RNC-H_2−CO. (d1 and d2) Pt−Cu CNC-as synthesized. (e1 and e2) Pt−Cu CNC-H_2. (f1 and f2) Pt−Cu CNC-H_2−CO. In the EDX line scans, blue and gray lines represent the atomic fractions of Cu and Pt. Note: the locations of blue and gray spots of these structural models do not represent the position of Cu and Pt atoms on surface of these nanocube catalysts; these images do not provide atomically precise information on the location of the constituting elements of Pt−Cu nanocubes. The level of details presented by the schematics of structural model does not represent the actual level of details achieved from the STEM characterization. The STEM characterization does not reach the details of the schematic.

Notably, there is no such Cu-rich subsurface in the Pt−Cu RNC-as synthesized (Figure 6a1). Such a sharp increase of Cu concentration and a simultaneous decrease of Pt concentration at the same location of the subsurface show that a Cu-rich subsurface is definitely formed. Figure S9 provides examples of the formation of Cu-rich subsurface in other Pt−Cu RNC-H_2 nanoparticles. Therefore, EDX of HAADF-STEM revealed that Cu atoms of surface layers migrate to subsurface and aggregate at the subsurface and thus form a Cu-rich subsurface.

3.2.3. Formation of Cu-Rich Region Is Supported by In Situ EXAFS. The migration of Cu atoms with a following aggregation to form Cu-rich layers in the subsurface of Pt−Cu RNC-H_2 is consistent with picture that emerges from the in situ EXAFS studies. Figures 7 and 8 presents the k^2-weighted Pt L_3-edge and Cu K-edge EXAFS spectra and the Fourier transform magnitudes of (a) the Pt−Cu RNC-as synthesized, (b) Pt−Cu RNC-H_2, (c) Pt−Cu CNC-as synthesized, (d) Pt−Cu CNC-H_2, and (e) Pt−Cu RNC-H_2−CO. Table 2 lists the coordination numbers (CN) of Cu−M and Pt−M (M: Cu, Pt)

DOI: 10.1021/acscatal.6b02054
ACS Catal. 2017, 7, 191−204

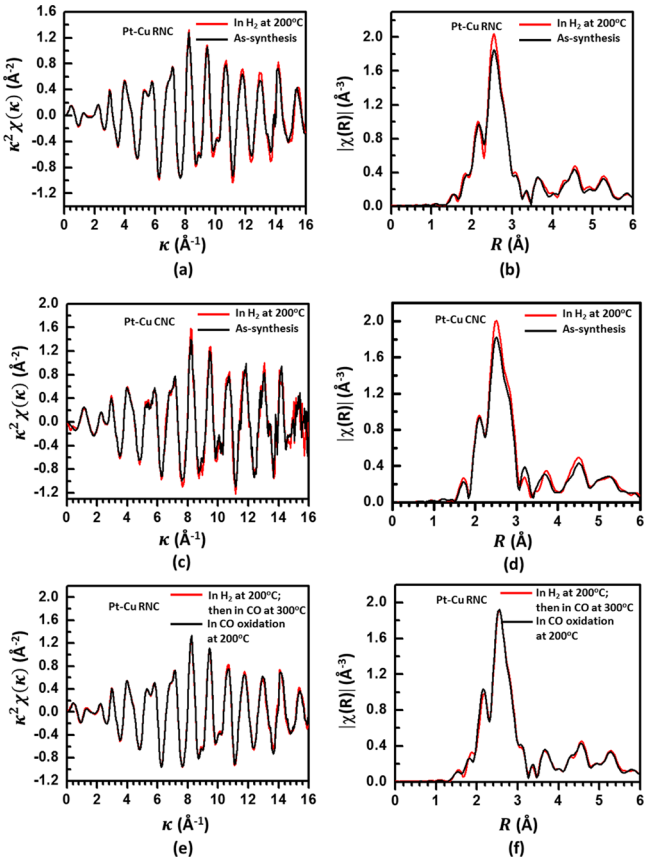

Figure 7. Pt-L_3 edge measured through in situ EXAFS studies of Pt−Cu RNC-as synthesized and Pt−Cu CNC-as synthesized and those under different reaction conditions. (a) κ^2-weighted Pt-L_3-edge EXAFS spectra in *k*-space for Pt−Cu RNC; (b) Fourier transform magnitude for Pt−Cu RNC; black line: the Pt−Cu RNC-as synthesized sample in air at room temperature (step 1); red line: Pt−Cu RNC-H_2 (step 2). (c) κ^2-weighted Pt-L_3-edge EXAFS spectra in *k*-space for Pt−Cu CNC; (d) Fourier transform magnitude for Pt−Cu CNC; black line: the Pt−Cu CNC-as synthesized sample in air at room temperature (step 1); red line: Pt−Cu CNC-H_2 (step 2). (e) κ^2-weighted Pt-L_3-edge EXAFS spectra in *k*-space for Pt−Cu RNC; (f) Fourier transform magnitude for Pt−Cu RNC; black line: the Pt−Cu RNC-H_2−CO; Red line: Pt−Cu RNC-H_2−CO during CO oxidation. All data were collected at room temperature after the treatment at high temperature as labeled in each figure.

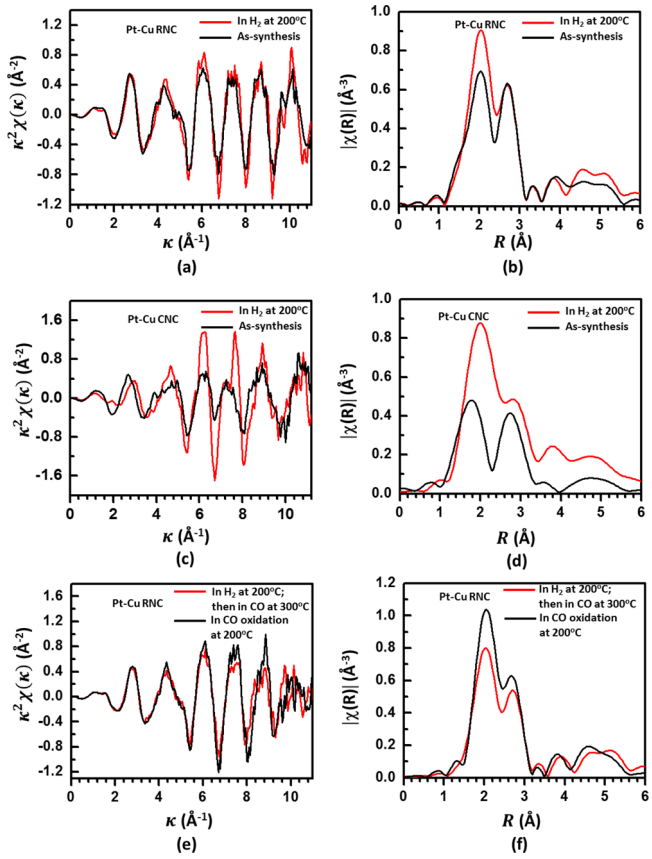

Figure 8. Cu K-edge measured through in situ EXAFS studies of Pt−Cu RNC-as synthesized and Pt−Cu CNC-as synthesized and those under different reaction conditions. (a) κ^2-weighted Cu K-edge EXAFS spectra in *k*-space for Pt−Cu RNC; (b) Fourier transform magnitude for Pt−Cu RNC; black line: the Pt−Cu RNC-as synthesized sample in air at room temperature (step 1); red line: Pt−Cu RNC-H_2 (step 2). (c) κ^2-weighted Cu K-edge EXAFS spectra in k-space for Pt−Cu CNC; (d) Fourier transform magnitude for Pt−Cu CNC; black line: the Pt−Cu CNC-as synthesized sample in air at room temperature (step 1); red line: Pt−Cu CNC-H_2 (step 2). (e) κ^2-weighted Cu K-edge EXAFS spectra in k-space for Pt−Cu RNC; (f) Fourier transform magnitude for Pt−Cu RNC; black line: the Pt−Cu RNC-H_2−CO; Red line: Pt−Cu RNC-H_2−CO during CO oxidation. All data were collected at room temperature after the treatment at high temperature as labeled in each figure.

and the corresponding bond lengths of the two catalysts treated under different conditions. The measured low coordination number of Cu around Cu atoms, CN(Cu−Cu), 2.9 ± 1.2 in the Pt−Cu RNC-as synthesized (entry 1 of Table 2), suggests the lack of a Cu-rich layer in Pt−Cu RNC-as synthesized catalyst before annealing at 200 °C in H_2. It is consistent with its EDX line scan (Figure 6a1). Importantly, the obvious significant increase of coordination number of CN(Cu−Cu) from 2.9 ± 1.2 of the Pt−Cu RNC-as synthesized to 4.4 ± 1.8 of the Pt−Cu RNC-H_2 (entry 5 in Table 2) is consistent with the formation of Cu-rich layers after the reaction in H_2 at 200 °C. In addition, the simultaneous decrease of CN(Cu−Pt) along with the increase of CN(Cu−Cu) (Figure 9b) confirm the formation of Cu-rich region for Pt−Cu RNC-H_2. Together, the combination of complementary information on EDX line scan, in situ EXAFS and AP-XPS, points toward the formation of Cu-rich atomic layers at near surface region of Pt−Cu RNC-as synthesized after reaction in H_2 at 200 °C, as schematically shown in Figure 1d.

3.2.4. DFT-Assisted Understanding of the Formation of Subsurface Alloy. To assist the understanding of the migration of Cu atoms from surface layers to the subsurface in H_2 at 200 °C, both the migration of Cu atoms from surface to subsurface and the segregation of Cu atoms from subsurface to surface in a hydrogen-covered Pt−Cu RNC were calculated with DFT. To determine what hydrogen coverage should be used for this calculation, Ab initio phase diagrams were constructed to determine the coverage of adsorbates used to calculate segregation energies in this work (Figures S10−S12); the details of these calculations can be found in the experimental section of the main text and the Supporting Information. Ab initio phase diagram for H adsorption on the reference configuration of PtCu (100) at different hydrogen coverages (Figure S10 and Table S2) suggests that the most stable phase is the surface covered with 1 ML of hydrogen atoms.

DOI: 10.1021/acscatal.6b02054
ACS Catal. 2017, 7, 191−204

Table 2. Coordination Environment (Coordination Numbers, Bond Lengths, and Their Mean Squared Disorder Values) of Cu and Pt Atoms of Pt−Cu RNC-As Synthesized and Pt−Cu CNC-As Synthesized in Different Reactant Gases (H_2, CO, Mixture of CO and O_2)[a]

entry	sample/condition	M_1-M_2	$CN(M_1-M_2)$	R (Å)	σ^2 (Å^2)	ΔE (eV)
1	Pt−Cu RNC at 25 °C in ambient ***Pt−Cu RNC-as synthesized***	Cu−Cu	2.9 ± 1.2	2.44 ± 0.03	0.012 ± 0.004	−7.9 ± 1.2
2		Cu−Pt	7.6 ± 1.6	2.69 ± 0.01	0.005 ± 0.002	−7.9 ± 1.2
3		Pt−Cu	1.0 ± 0.4	2.69 ± 0.01	0.005 ± 0.002	10.0 ± 0.3
4		Pt−Pt	9.5 ± 0.5	2.748 ± 0.002	0.0057 ± 0.0001	10.0 ± 0.3
5	Pt−Cu RNC at 200 °C in H_2 ***Pt−Cu RNC-H_2***	Cu−Cu	4.4 ± 1.8	2.50 ± 0.03	0.012 ± 0.004	−5.8 ± 1.8
6		Cu−Pt	5.5 ± 1.6	2.72 ± 0.01	0.004 ± 0.002	−5.8 ± 1.8
7		Pt−Cu	0.7 ± 0.3	2.72 ± 0.01	0.004 ± 0.002	10.0 ± 0.3
8		Pt−Pt	10.3 ± 0.4	2.748 ± 0.002	0.0057 ± 0.0001	10.0 ± 0.3
9	Pt−Cu RNC at 300 °C in CO after H_2-200 °C ***Pt−Cu RNC-H_2-CO***	Cu−Cu	4.2 ± 1.7	2.53 ± 0.03	0.012 ± 0.004	−6.2 ± 1.6
10		Cu−Pt	6.1 ± 1.7	2.70 ± 0.01	0.006 ± 0.003	−6.2 ± 1.6
11		Pt−Cu	1.1 ± 0.5	2.70 ± 0.01	0.006 ± 0.003	10.0 ± 0.3
12		Pt−Pt	9.8 ± 0.5	2.749 ± 0.002	0.0057 ± 0.0001	10.0 ± 0.3
13	Pt−Cu RNC-H_2−CO in mixture of CO+O_2	Cu−Cu	3.3 ± 1.3	2.51 ± 0.03	0.012 ± 0.004	−6.6 ± 1.4
14		Cu−Pt	5.8 ± 1.4	2.71 ± 0.01	0.006 ± 0.003	−6.6 ± 1.4
15		Pt−Cu	0.9 ± 0.4	2.71 ± 0.01	0.006 ± 0.003	10.0 ± 0.3
16		Pt−Pt	9.8 ± 0.5	2.751 ± 0.002	0.0057 ± 0.0001	10.0 ± 0.3
17	Pt−Cu CNC at 25 °C in ambient ***Pt−Cu RNC-as synthesized***	Cu−Cu	4.9 ± 0.6	2.42 ± 0.01	0.009 ± 0.001	−7.6 ± 1.0
18		Cu−Pt	7.5 ± 0.9	2.72 ± 0.01	0.003 ± 0.002	−7.6 ± 1.0
19		Pt−Cu	0.8 ± 0.4	2.72 ± 0.01	0.003 ± 0.002	10.3 ± 0.7
20		Pt−Pt	9.7 ± 1.2	2.745 ± 0.005	0.0055 ± 0.0005	10.3 ± 0.7
21	Pt−Cu CNC at 200 °C in H_2 ***Pt−Cu CNC-H_2***	Cu−Cu	5.9 ± 0.7	2.53 ± 0.02	0.009 ± 0.001	−4.1 ± 1.7
22		Cu−Pt	3.4 ± 1.0	2.72 ± 0.02	0.002 ± 0.003	−4.1 ± 1.7
23		Pt−Cu	0.8 ± 0.6	2.72 ± 0.02	0.002 ± 0.003	10.3 ± 0.7
24		Pt−Pt	10.4 ± 1.2	2.748 ± 0.006	0.0055 ± 0.0005	10.3 ± 0.7
25	Pt−Cu CNC at 300 °C in CO after H_2-200 °C ***Pt−Cu CNC-H_2-CO***	Cu−Cu	6.7 ± 1.0	2.54 ± 0.01	0.009 ± 0.001	−6.4 ± 1.6
26		Cu−Pt	1.3 ± 0.8	2.64 ± 0.01	0.002 ± 0.004	−6.4 ± 1.6
27		Pt−Cu	1.0 ± 0.7	2.64 ± 0.01	0.002 ± 0.004	10.3 ± 0.7
28		Pt−Pt	10.5 ± 1.2	2.760 ± 0.005	0.0055 ± 0.0005	10.3 ± 0.7

[a]All results correspond to the room temperature at which EXAFS data were collected. The last column contains the best fit values of the photoelectron energy origin correction.

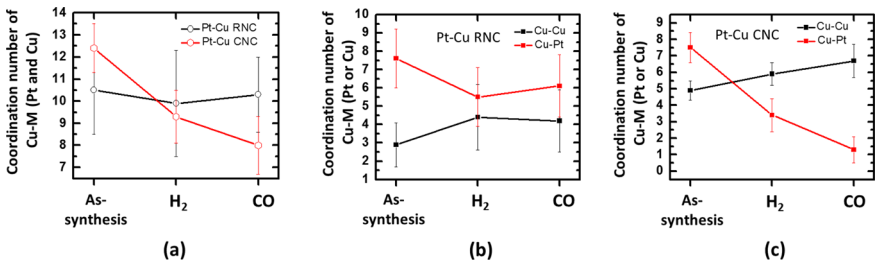

Figure 9. Evolution of coordination environment of Cu and Pt atoms of Pt−Cu RNC and Pt−Cu CNC along the sequence of as-synthesized, reaction in H_2, and reaction in CO. (a) Total coordination number of Cu atoms, CN(Cu−M) (CN(Cu−M) = CN(Cu−Cu)+CN(Cu−Pt)). (b) Coordination numbers of CN(Cu−Cu) and CN(Cu−Pt) of Pt−Cu RNC. (c) Coordination numbers of CN(Cu−Cu) and CN(Cu−Pt) of Pt−Cu CNC.

In these calculations, a structure with a 25% concentration of Cu atoms in the second layer was chosen as a reference state (Figure 10a,b). In this reference structural model, there are no Cu atoms initially presented in the third layer. With this reference state, the calculated segregation energy for segregating Cu atoms from the second layer to the surface is 0.40 eV (entry 3 in Table S2). Thus, it would be thermodynamically unfavorable if Cu atoms in the second layer could segregate to the topmost layer; in other words, segregation of Cu atoms present on the surface of Pt−Cu RNC-as synthesized to the subsurface is thermodynamically favorable. In addition, the energy change by migrating Cu atoms from the second layer to the third layer is slightly exothermic, at −0.07 eV. These calculations suggest that Cu atoms prefer to be in the subsurface region of Pt−Cu RNC-H_2, consistent with the formation of a Cu-rich subsurface in Pt−Cu RNC-H_2 identified with the above experimental studies.

3.2.5. Stability of Pt−Cu RNC-H_2 Generated from Treatment in H_2. The Pt−Cu RNC-H_2 is highly active for CO oxidation. Careful kinetic studies (Figure 4 and Figuress S1−S5) show that the activation barrier for CO oxidation on this surface is only 39−41 kJ/mol. In situ studies of the surface of Pt−Cu RNC-H_2 during CO oxidation at 25−240 °C revealed that its surface composition and oxidation state during CO oxidation at a temperature up to about 240 °C remain the same as Pt−Cu RNC-H_2 before CO oxidation (Figure 5b). These

DOI: 10.1021/acscatal.6b02054
ACS Catal. 2017, 7, 191−204

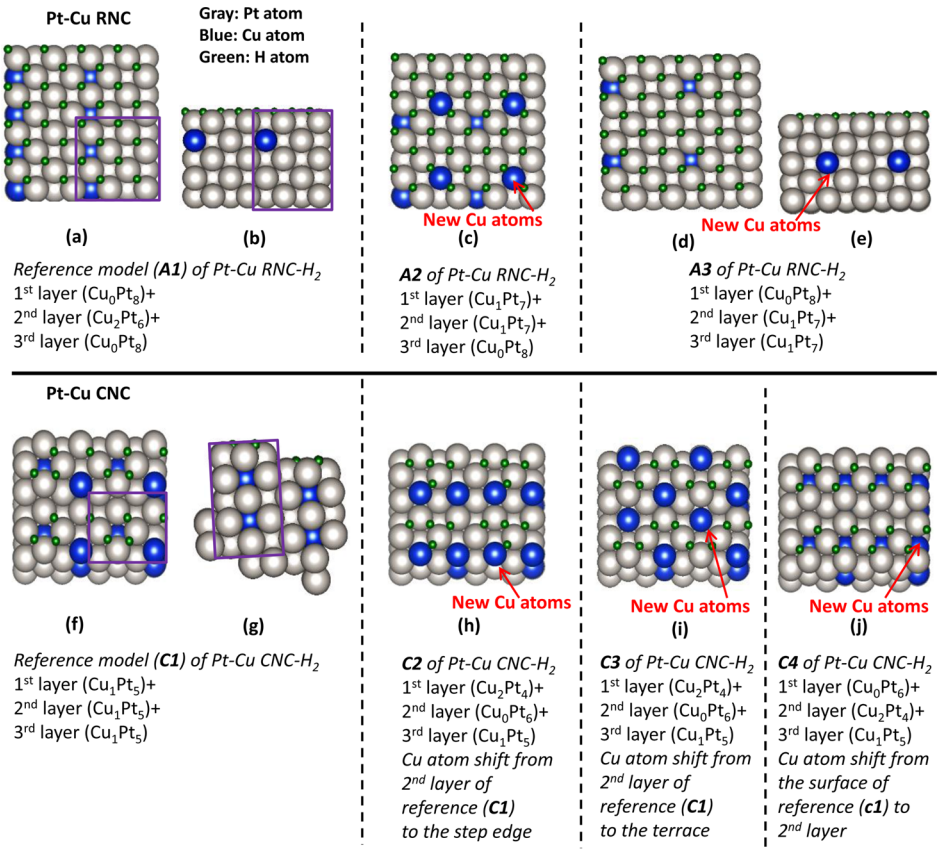

Figure 10. Optimized structural models of Pt−Cu RNC in H_2 and Pt−Cu CNC in H_2 by using periodic DFT calculation. (a) Top view of reference model of structural A1 of Pt−Cu RNC with adsorbed H atoms used as a starting structure. (b) Side view of reference model A1 of Pt−Cu RNC with adsorbed H atoms. (c) Top view of structural model A2 of Pt−Cu RNC with adsorbed H atoms, in which Cu atoms of the second layer segregate to surface. (d) Top view of structural model A3 of Pt−Cu RNC with adsorbed H atoms, in which Cu atoms of the second layer migrate to the third layer. (e) Side view of structural model A3 of Pt−Cu RNC with adsorbed H atoms, in which Cu atoms of the second layer migrate to the third layer. (f) Top view of reference model C1 of Pt−Cu CNC with adsorbed H atoms. (g) Side view of reference model C1 of Pt−Cu CNC with adsorbed H atoms. (h) Top view of structural model C2 of Pt−Cu CNC with adsorbed H atoms, in which Cu atoms of the second layer shift to the step edge. (i) Top view of structural model C3 of Pt−Cu CNC with adsorbed H atoms, in which Cu atoms of the second layer shift to the terrace. (j) Top view of structural model C4 of Pt−Cu CNC with adsorbed H atoms, in which Cu atoms on the surface migrate to the second layer.

results, in turn, suggest that the catalyst surface formed in gas phase H_2 at 200 °C is thermodynamically stable in the subsequent CO oxidation at a temperature up to 240 °C.

The obvious decrease of activation barrier of CO oxidation on Pt−Cu RNC-H_2 illustrates that a postsynthesis reaction in a gas phase is a new approach for developing a catalyst with superior catalytic performance. This significant decrease of activation barrier for CO oxidation on Pt−Cu RNC-H_2 is closely relevant to the largely decreased binding energy of CO molecules on Pt atoms of the near surface alloy consisting of Pt skip layers and Cu-rich subsurface.[37] To test the durability of catalytic activity of CO oxidation on Pt−Cu RNC-H_2, we prepared a catalyst termed Pt−Cu RNC-H_2−CO oxidation-H_2 by annealing Pt−Cu RNC-H_2−CO oxidation at 200 °C in H_2; now this catalyst is termed Pt−Cu RNC-H_2−CO oxidation-H_2; kinetics studies of CO oxidation in the temperature range of 175 °C-200 °C on Pt−Cu RNC-H_2−CO oxidation-H_2 was performed. The measured activation barrier of CO oxidation on this catalyst is 32 kJ/mol (Figure S13), very close to the activation barrier (39 kJ/mol) of Pt−Cu RNC-H_2. In addition, the catalyst after the third treatment at 200 °C in hydrogen (termed Pt−Cu RNC-H_2−CO oxidation-H_2−CO oxidation-H_2) exhibits an activation barrier of 37 kJ/mol. The preservation of activation barrier of Pt−Cu RNC-H_2 after three cycles of H_2 treatment and CO oxidation suggests that surface chemistry and structure of Pt−Cu RNC-H_2 remain unchanged after three cycles of H_2 treatment and CO oxidation. It is confirmed by AP-XPS studies (Figure S14). The kinetics studies and measurements of surface chemistry of Pt−Cu RNC-H_2 in three cycles of reactions in H_2 and CO oxidation suggest the high thermal stability and catalytic durability of the catalyst Pt−Cu RNC-H_2.

3.3. Formation of a New Surface on Pt−Cu RNC through Sequential Reactions in Different Gases. To explore the possibility of developing a new bimetallic catalyst through sequential postsynthesis reactions in different gases, a second postsynthesis reaction for Pt−Cu RNC-H_2 in CO at 350 °C was performed. Upon the second postsynthesis reaction, the formed catalysts are termed Pt−Cu RNC-H_2−CO. Figure 5c shows the evolution of atomic fractions of Cu and Pt of Pt−Cu RNC-as synthesized in sequential reactions (1) in H_2 at 200 °C, (2) in pure CO at different temperatures up to 350 °C, and (3) in the mixture of CO and O_2 for CO oxidation at 260 °C. Notably, the atomic fraction of Cu of Pt−Cu RNC-H_2 increases from 1.0% to 9.5% upon the second reaction at 350 °C in gas phase of CO. To confirm that the change of surface composition of Pt−Cu RNC-H_2 in CO (Figure 5c) results from annealing in CO instead of thermal

DOI: 10.1021/acscatal.6b02054
ACS Catal. 2017, 7, 191−204

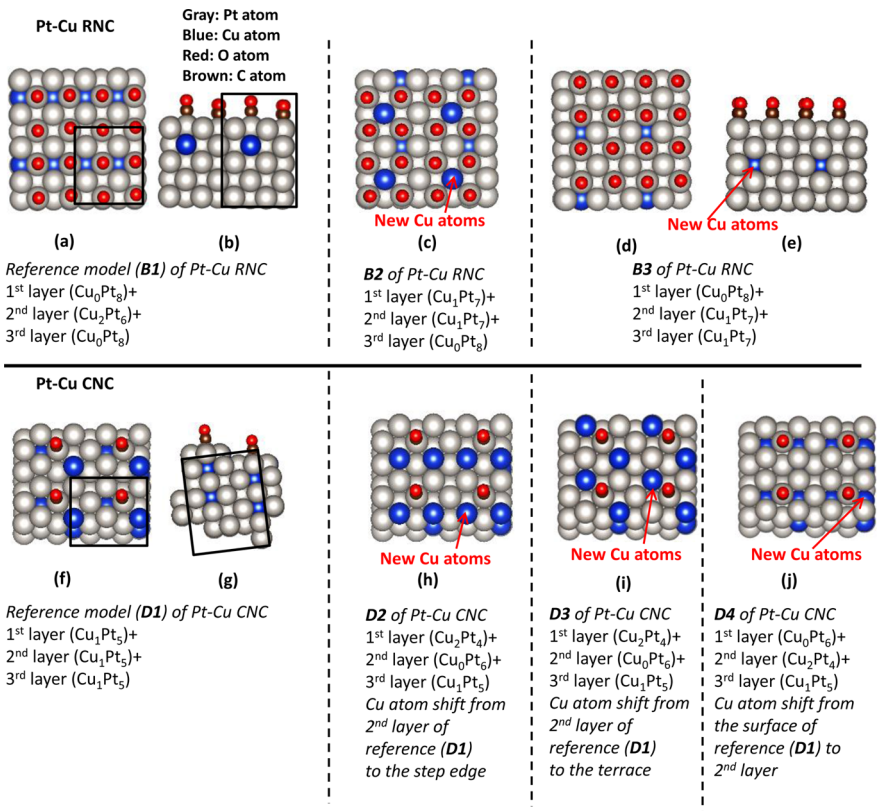

Figure 11. Optimized structural models of Pt−Cu RNC in CO and Pt−Cu CNC in CO by using periodic DFT calculation. (a) Top view of reference model of structural B1 of Pt−Cu RNC with adsorbed CO molecules used as a starting structure; the compositions of the first, second, and third layers are Cu_0Pt_8, Cu_2Pt_6, and Cu_0Pt_8. (b) Side view of reference model B1 of Pt−Cu RNC with adsorbed CO molecules. (c) Top view of structural model B2 of Pt−Cu RNC with adsorbed CO molecules, in which Cu atoms of the second layer segregate to surface. (d) Top view of structural model B3 of Pt−Cu RNC with adsorbed CO molecules, in which Cu atoms of the second layer migrate to the third layer. (e) Side view of structural model B3 of Pt−Cu RNC with adsorbed CO molecules, in which Cu atoms of the second layer migrate to the third layer. (f) Top view of reference model D1 of Pt−Cu CNC with adsorbed CO molecules. (g) Side view of reference model D1 of Pt−Cu CNC with adsorbed CO molecules. (h) Top view of structural model D2 of Pt−Cu CNC with adsorbed CO molecules, in which Cu atoms of the second layer shift to the step edge. (i) Top view of structural model D3 of Pt−Cu CNC with adsorbed CO molecules, in which Cu atoms of the second layer shift to the terrace. (j) Top view of structural model D4 of Pt−Cu CNC with adsorbed CO molecules, in which Cu atoms on surface migrate to the second layer.

diffusion of metal atoms at 350 °C, Pt−Cu RNC-H_2 was annealed at 425 °C in pure N_2 at the same pressure as CO. In situ AP-XPS studies showed that the surface composition of Pt−Cu RNC-N_2 is the same as Pt−Cu RNC-as synthesized but different from Pt−Cu RNC-H_2−CO. Thus, the increase of concentration of Cu in Pt−Cu RNC-H_2−CO (compared to Pt−Cu RNC-H_2) results from the treatment in gas phase of CO instead of thermal diffusion.

Compared to Pt−Cu RNC-H_2 (Figure 6b1), Pt−Cu RNC-H_2−CO does not have a Cu-rich subsurface layer (Figure 6c1). It suggests that the Cu-rich layers at subsurface of Pt−Cu RNC-H_2 have diffused during annealing at 350 °C in CO. The increase of Cu concentration of Pt−Cu RNC-H_2−CO revealed by AP-XPS (Figure 5c) suggests the segregation of Cu atoms from Cu-rich subsurface of Pt−Cu RNC-H_2 to topmost layers of Pt−Cu RNC-H_2−CO.

DFT calculations of the segregation energies of Cu atoms of Pt−Cu RNC-H_2 covered with CO molecules were performed to aid the understanding for the segregation of Cu to the topmost layer of Pt−Cu RNC-H_2−CO. Segregation or migration energies of Cu atom of PtCu (100) in a CO environment were calculated with DFT. A reference structure was built in Figure 11a,b. In this reference structure, the compositions of the first, second, and third layer are Cu_0Pt_8, Cu_2Pt_6, and Cu_0Pt_8, respectively. The energies for (1) segregating Cu atoms from the second layer to the surface (Figure 11c) and for (2) migrating Cu atoms from the second layer to the third layer (Figures 11d and 11e) are −0.11 eV (entry 3 in Table S3) and 0.13 eV (entry 4 in Table S3), respectively. Thus, the segregation of Cu atoms from subsurface to topmost surface in CO is thermodynamically favorable.

These analyses suggest that the Cu of Cu-rich subsurface of Pt−Cu RNC-H_2 segregates to the topmost surface of Pt−Cu RNC-H_2−CO in CO, forming a Pt−Cu alloy on surface. Activation barrier for CO oxidation on Pt−Cu RNC-H_2−CO was measured. Activation barrier of Pt−Cu RNC-H_2−CO (173 ± 11 kJ/mol) is much higher than Pt−Cu RNC-H_2, 39 ± 4 kJ/mol; this significant increase of activation barrier must result from a change of surface structure of Pt−Cu RNC-H_2 in CO. This high activation barrier is consistent with theoretical studies in literature; high activation barrier of Pt−Cu alloy was predicted in the literature.[16] The significant change of catalytic performance clearly suggested that catalytic performance of a bimetallic catalyst can be tuned through sequential reactions in gas phases.

3.4. Structure of Pt−Cu CNC-H_2 Formed through a Postsynthesis Reaction in H_2 and Its Correlation to Catalytic Performance. Compared to the flat (100) surface

DOI: 10.1021/acscatal.6b02054
ACS Catal. 2017, 7, 191−204

of the Pt−Cu RNC-as synthesized, the Pt−Cu CNC-as synthesized has a stepped surface (Figure 3). Kinetic studies for CO oxidation on Pt−Cu CNC-based catalysts were studied under the same catalytic condition as Pt−Cu RNC-based catalysts. The activation energy of CO oxidation on the Pt−Cu CNC-as synthesized without any treatment (109 ± 10 kJ/mol) (Figure 4 and Table 1) is similar to that of pure Pt regular nanocubes upon H_2 treatment at 200 °C (Pt-RNC-H_2) (92 ± 5 kJ/mol). Upon reaction with H_2 at 200 °C, the activation energy on the newly formed surface, Pt−Cu CNC-H_2 is about 72 ± 6 kJ/mol (Figure 4). The quite low concentration of Cu (atomic fraction of Cu: $F_{Cu} = \frac{Cu}{Cu + Pt} = 4\%$) on surface of Pt−Cu CNC-H_2 makes the surface exhibit an activation barrier (72 ± 6 kJ/mol) approximately similar to pure Pt RNC-H_2 (92 ± 5 kJ/mol).

In contrast to the significant decrease of the activation barrier of Pt−Cu RNC-as synthesized (128 ± 7 kJ/mol) to 39 ± 4 kJ/mol of Pt−Cu RNC-H_2, there is no significant difference between activation barrier of the Pt−Cu CNC-as synthesized (109 ± 10 kJ/mol) and that of Pt−Cu CNC-H_2 (72 ± 6 kJ/mol) (Table 1). In situ AP-XPS studies of Pt−Cu CNC-H_2 during CO oxidation were performed to elucidate why the catalytic performance of Pt−Cu CNC-H_2 (72 ± 6 kJ/mol) is distinctly different from that of Pt−Cu RNC-H_2 (39 ± 4 kJ/mol). As shown in Figure 5b, the atomic fraction of Cu of Pt−Cu RNC-as synthesized is decreased from ∼19% to 1% upon annealing at 200 °C in H_2; however, Cu fraction of Pt−Cu CNC-as synthesized is decreased from 9% to 4% (Figure 5e) upon the same annealing. EDX line scan suggests that Pt−Cu CNC-H_2 (Figure 6e1) does not have a Cu-rich subsurface in Pt−Cu CNC-H_2 although a Cu-rich surface was clearly observed in Pt−Cu RNC-H_2 (Figure 6b1); thus, the lack of subsurface Cu-rich surface in the case of Pt−Cu−CNC-H_2 made it behave similar to Pt nanocubes.

The distinct difference in catalytic performance between the catalyst surfaces of Pt−Cu RNC-H_2 and Pt−Cu CNC-H_2 suggests an obvious difference in the capability of responding to the annealing at 200 °C in H_2 between Pt−Cu RNC-as synthesized and Pt−Cu CNC-as synthesized. This is the insight we gained from the parallel studies of Pt−Cu RNC and Pt−Cu CNC in the reaction at with H_2 at 200 °C and their catalytic performance of the resulted catalyst surfaces.

3.5. Surface of Pt−Cu CNC Experiencing Sequential Reactions in Different Gases. Pt−Cu CNC-H_2−CO was prepared by annealing Pt−Cu CNC-H_2 in CO at 350 °C. Kinetic studies for CO oxidation on Pt−Cu CNC-H_2−CO show that the activation barrier is 80 ± 8 kJ/mol (Table 1). This is very similar to the activation barrier of CO oxidation on Pt−Cu CNC-H_2 (Table 1), 72 ± 6 kJ/mol. It is somewhat close to the activation barrier of Pt RNC-H_2, 92 ± 5 kJ/mol (entry 1 of Table 1). The similarity in activation energies of CO oxidation on Pt−Cu CNC-H_2−CO (80 ± 8 kJ/mol) and pure Pt RNC-H_2 (92 ± 5 kJ/mol) suggests that packing of Pt atoms on the topmost layer of Pt−Cu CNC-H_2−CO is similar to a pure Pt surface of a Pt RNC-H_2.

Surprisingly, Pt−Cu CNC-H_2−CO during CO oxidation at 260 °C (Figure 5f) has concentration of Cu similar to Pt−Cu RNC-H_2−CO (Figure 5c) though they gave distinctly different activation barriers, 80 ± 8 kJ/mol of Pt−Cu CNC-H_2−CO versus 173 ± 11 kJ/mol of Pt−Cu RNC-H_2−CO. In fact, the surface structures of Pt−Cu RNC-H_2−CO and Pt−Cu CNC-H_2−CO are actually quite different although the Cu concentrations of the two catalysts are very similar. As shown in the red line of Figure 9a, the total coordination number of Cu atoms of Pt−Cu CNC, CN(Cu−M, M = Pt, Cu) is surprisingly decreased when the pretreatment gas was changed from H_2 to CO, distinctly from the preservation in the case of Pt−Cu RNC (dark line). In principle, CN(Cu−M) should remain unchanged because both Cu and Pt atoms pack into a face-centered cubic (fcc) lattice. The obvious decrease of CN(Cu−M) suggests that Cu atoms segregate to surface and form Cu nanoclusters; the low CN(Cu−M) of these exposed Cu nanoclusters on topmost surface protruding to vacuum makes the average CN(Cu−M) decrease. This hypothesis was further supported by the increase of CN(Cu−Cu) and simultaneous decrease of CN(Cu−Pt) (Figure 9c). The segregation of Cu atoms which aggregate to form Cu nanoclusters on surface of Pt−Cu CNC-H_2−CO is also supported by the increase of Cu concentration in the surface region based on AP-XPS studies when Pt−Cu CNC-H_2 was being annealed at 350 °C in CO (Figure 5f).

The high barrier for CO oxidation on Pt−Cu RNC-H_2−CO results from the formation of Pt−Cu alloy of the catalyst surface; on this catalyst surface, the CO adsorption energy is largely enhanced due to electron transfer from Cu to Pt on the surface.[16] For Pt−Cu CNC-H_2−CO, however, its activation barrier is similar to the pure Pt-RNC-H_2, which suggests that its Cu atoms could exist in the format of Cu-nanoclusters instead of randomly alloying with Pt atoms. This suggestion of formation of Cu nanoclusters was supported by the results of EXAFS studies in Figure 9. This is further supported by the increase of atomic fraction of Cu in surface region from 4% of Pt−Cu CNC-H_2 to 11% of Pt−Cu CNC-H_2−CO (Figure 5f). Based on these studies, Pt atoms exist in the format of Pt patches, by which the activation barrier of Pt−Cu CNC-H_2−CO is similar to pure Pt RNC-H_2 (Table 1). A structural model at the right side in Figure 5f schematically shows the formation of Cu nanoclusters.

DFT calculations were performed to aid the understanding for the observed segregation of Cu to the topmost layer of Pt−Cu CNC-H_2−CO. Segregation energies of Cu atoms on a stepped surface of PtCu in a CO environment were calculated by using a PtCu (310) model with adsorbed CO molecules. A stepped bimetallic surface with adsorbed CO molecules was constructed as a reference structure (Figure 11f,g). In this reference structure, the composition of each of the first, second, and third layer is Cu_1Pt_5. As shown in entry 9 in Table S3, the migration of Cu atoms from the surface of Pt(310) to the second layer of Pt−Cu CNC-H_2−CO is unfavorable (ΔE = 0.15 eV) when CO is adsorbed on the surface. However, the segregation energy, ΔE, for segregating Cu atoms from the second layer to the step edge of PtCu (310) (with absorbed CO molecules) is −0.21 eV (entry 7 in Table S3); thus, segregation of Cu atoms from the second layer to step edge is energetically favorable. Notably, segregation of Cu atoms from the second layer to a terrace of PtCu(310) is thermodynamically unfavorable, with a ΔE of 0.26 eV (entry 8 in Table S3). Thus, the energetically favorable segregation of Cu atoms from the second layer to step edge of PtCu (310) of Pt−Cu CNC-H_2 in CO suggests that Pt atoms at step edges of Pt−Cu CNC-H_2 in CO will be replaced with the segregated Cu atoms. As these Cu atoms at step edges have a coordination number of 7 or less, they aggregate on surface and thus form Cu nanoclusters to decrease their surface energy. Thus, these

DOI: 10.1021/acscatal.6b02054
ACS Catal. 2017, 7, 191−204

calculations well-rationalized why Cu atoms segregated to surface to form Cu nanoclusters.

4. SUMMARY

Pt−Cu RNC-as synthesized and Pt−Cu CNC-as synthesized were used as two probe catalysts in the demonstration of tunability of catalytic performance of bimetallic catalysts through postsynthesis reaction(s) in gas phase(s). Postsynthesis reactions in different reaction conditions including (a) only H_2 at 200 °C, (b) first H_2 at 200 °C and then CO at 350 °C (H_2 →CO) were performed. In situ characterizations of surface chemistry with AP-XPS and of coordination environments of Cu and Pt atoms under reactions (H_2 or H_2 → CO) or during catalysis (CO oxidation after reaction in H_2 or H_2 → CO) with EXAFS studies showed that a different catalyst surface and structure was formed in reaction with one or more gases. The resulting new catalytic performances were revealed with kinetics studies of these formed new catalyst structures. Annealing of Pt−Cu RNC-as synthesized in H_2 at 200 °C generates a near surface alloy which consists of a skin layer of pure Pt, a Cu-rich subsurface, and Pt-rich deep layers. Compared to pure Pt or Pt−Cu alloy nanoparticles, Cu atoms of Cu-rich subsurface significantly modify the electronic states of Pt atoms of the topmost surface layer where catalysis is performed. The significant decrease of adsorption energy of CO on skin layer Pt atoms supported on Cu-rich subsurface of the newly formed near subsurface alloy (Pt−Cu RNC-H_2) offers a quite low activation (39 ± 4 kJ/mol). This work demonstrated the capability of tuning catalytic performance of bimetallic catalyst nanoparticles through postsynthesis reaction in gas phase.

■ ASSOCIATED CONTENT

Supporting Information

The Supporting Information is available free of charge on the ACS Publications website at DOI: 10.1021/acscatal.6b02054.

Preparation of catalysts for kinetics studies; investigation of the influence of thickness of catalyst bed on kinetics studies; checking the metallic state of constituting metals of catalysts before and after CO oxidation; checking the accuracy of kinetics studies of CO oxidation; Iidentifying distributions of Pt and Cu from surface to core of Pt−Cu nanoparticles with high-angle annular dark-field scanning transmission electron microscopy (HAADF-STEM) technique; understanding the difference in activation barriers of Pt−Cu RNC-as synthesized and Pt−Cu CNC-as synthesized and those after postsynthesis reaction(s) in gas phase(s); understanding significant difference in activation barriers between Pt−Cu RNC-as synthesized and Pt−Cu RNC-H_2 versus small difference between Pt−Cu CNC-as synthesized and Pt−Cu CNC-H_2; measuring reaction orders of CO and O_2; evidence in support of the formation of Cu-rich layers in Pt−Cu RNC-H_2; DFT calculations of Pt−Cu (100) and (310) surface models; testing of stability of catalytic performances; measurements of surface composition at different reaction steps and stability of a restructured surface; identification of possibility of restructuring Pt−Cu surface with other reactant gases; representative EXAFS fits; supporting figures and tables (PDF)

■ AUTHOR INFORMATION

Corresponding Authors

*E-mail for A.I.F.: frenkel@bnl.gov.

*E-mail for F.T.: franklin.feng.tao@ku.edu.

Notes

The authors declare no competing financial interest.

■ ACKNOWLEDGMENTS

This work is supported by the Chemical Sciences, Geosciences and Biosciences Division, Office of Basic Energy Sciences, Office of Science, U.S. Department of Energy under Grant No. DE- SC0014561 awarded to F.T. A.I.F. and J.C.Y. acknowledge support from the U.S. Department of Energy Grant No. DE-FG02-03ER15476. We thank A. Chafé and A. Patlolla for assistance with the XAFS data acquisition. We acknowledge the facilities support provided at the NSLS at the Brookhaven National Laboratory (U.S. Department of Energy, Office of Basic Energy Sciences, Contract No. DE-SC0012704) and the Synchrotron Catalysis Consortium (U.S. Department of Energy, Office of Basic Energy Sciences, Grant No. DE-SC0012335) that supported operations at the SSRL (beamline BL2-2). J.G. acknowledges support through a DOE Early Career Award of the Chemical Sciences, Geosciences and Biosciences Division, Office of Basic Energy Sciences, Office of Science, U.S. Department of Energy.

■ REFERENCES

(1) Besenbacher, F.; Chorkendorff, I.; Clausen, B. S.; Hammer, B.; Molenbroek, A. M.; Norskov, J. K.; Stensgaard, I. D. *Science* **1998**, *279*, 1913−1915.

(2) Chen, M. S.; Kumar, D.; Yi, C. W.; Goodman, D. W. The promotional effect of gold in catalysis by palladium-gold. *Science* **2005**, *310*, 291−293.

(3) Chen, J. G.; Menning, C. A.; Zellner, M. B. *Surf. Sci. Rep.* **2008**, *63*, 201−254.

(4) Somorjai, G. A. *Chem. Rev.* **1996**, *96*, 1223−1235.

(5) Ferrando, R.; Jellinek, J.; Johnston, R. L. *Chem. Rev.* **2008**, *108*, 845−910.

(6) Rodriguez, J. A. *Surf. Sci. Rep.* **1996**, *24*, 223−287.

(7) Tao, F.; Dag, S.; Wang, L. W.; Liu, Z.; Butcher, D. R.; Bluhm, H.; Salmeron, M.; Somorjai, G. A. *Science* **2010**, *327*, 850−853.

(8) Tao, F.; Salmeron, M. *Science* **2011**, *331*, 171−174.

(9) Tao, F.; Grass, M. E.; Zhang, Y.; Butcher, D. R.; Renzas, J. R.; Liu, Z.; Chung, J. Y.; Mun, B. S.; Salmeron, M.; Somorjai, G. A. *Science* **2008**, *322*, 932−934.

(10) Divins, N. J.; Angurell, I.; Escudero, C.; Perez-Dieste, V.; Llorca, J. *Science* **2014**, *346*, 620−623.

(11) Hansgen, D. A.; Vlachos, D. G.; Chen, J. G. G. *Nat. Chem.* **2010**, *2*, 484−489.

(12) Zafeiratos, S.; Piccinin, S.; Teschner, D. *Catal. Sci. Technol.* **2012**, *2*, 1787−1801.

(13) Kitchin, J. R.; Norskov, J. K.; Barteau, M. A.; Chen, J. G. *J. Chem. Phys.* **2004**, *120*, 10240−10246.

(14) Fu, Q.; Yang, F.; Bao, X. H. *Acc. Chem. Res.* **2013**, *46*, 1692−1701.

(15) Mu, R. T.; Guo, X. G.; Fu, Q.; Bao, X. H. *J. Phys. Chem. C* **2011**, *115*, 20590−20595.

(16) Andersson, K. J.; Calle-Vallejo, F.; Rossmeisl, J.; Chorkendorff, L. *J. Am. Chem. Soc.* **2009**, *131*, 2404−2407.

(17) Bahn, S. R.; Jacobsen, K. W. *Comput. Sci. Eng.* **2002**, *4*, 56−66.

(18) Tao, F. *ChemCatChem* **2012**, *4*, 583−590.

(19) Shan, J. J.; Zhu, Y.; Zhang, S. R.; Zhu, T.; Rouvimov, S.; Tao, F. *J. Phys. Chem. C* **2013**, *117*, 8329−8335.

(20) Moulder, J. F. S., W, F.; Sobol, P. E.; Bomben, K. D.: *Handbook of X-ray Photoelectron Spectroscopy*; Perkin-Elmer Corporation: Waltham, MA, 1992.

DOI: 10.1021/acscatal.6b02054
ACS Catal. 2017, 7, 191−204

(21) Chupas, P. J.; Chapman, K. W.; Kurtz, C.; Hanson, J. C.; Lee, P. L.; Grey, C. P. *J. Appl. Crystallogr.* **2008**, *41*, 822−824.
(22) Clausen, B. S.; Steffensen, G.; Fabius, B.; Villadsen, J.; Feidenhansl, R.; Topsoe, H. I. *J. Catal.* **1991**, *132*, 524−535.
(23) Newville, M. *J. Synchrotron Rad.* **2001**, *8*, 322.
(24) Nashner, M. S.; Frenkel, A. I.; Adler, D. L.; Shapley, J. R.; Nuzzo, R. G. S. *J. Am. Chem. Soc.* **1997**, *119*, 7760−7771.
(25) Frenkel, A. I.; Hills, C. W.; Nuzzo, R. G. *J. Phys. Chem. B* **2001**, *105*, 12689−12703.
(26) Frenkel, A. *Z. Kristallogr. - Cryst. Mater.* **2007**, *222*, 605−611.
(27) Frenkel, A. I. *Chem. Soc. Rev.* **2012**, *41*, 8163−8178.
(28) Frenkel, A. I.; Yevick, A.; Cooper, C.; Vasic, R. *Annu. Rev. Anal. Chem.* **2011**, *4*, 23−39.
(29) Enkovaara, J.; Rostgaard, C.; Mortensen, J. J.; Chen, J.; Dulak, M.; Ferrighi, L.; Gavnholt, J.; Glinsvad, C.; Haikola, V.; Hansen, H. A.; Kristoffersen, H. H.; Kuisma, M.; Larsen, A. H.; Lehtovaara, L.; Ljungberg, M.; Lopez-Acevedo, O.; Moses, P. G.; Ojanen, J.; Olsen, T.; Petzold, V.; Romero, N. A.; Stausholm-M?ller, J.; Strange, M.; Tritsaris, G. A.; Vanin, M.; Walter, M.; Hammer, B.; Hakkinen, H.; Madsen, G. K. H.; Nieminen, R. M.; Norskov, J.; Puska, M.; Rantala, T. T.; Schiotz, J.; Thygesen, K. S.; Jacobsen, K. W. *J. Phys.: Condens. Matter* **2010**, *22*, 253202.
(30) Mortensen, J. J.; Hansen, L. B.; Jacobsen, K. W. *Phys. Rev. B: Condens. Matter Mater. Phys.* **2005**, *71*, 1−8.
(31) Kresse, G.; Joubert, D. *Phys. Rev. B: Condens. Matter Mater. Phys.* **1999**, *59*, 1758−1775.
(32) Blochl, P. E. *Phys. Rev. B: Condens. Matter Mater. Phys.* **1994**, *50*, 17953−17979.
(33) Hammer, B.; Hansen, L. B.; Norskov, J. K. *Phys. Rev. B: Condens. Matter Mater. Phys.* **1999**, *59*, 7413−7421.
(34) Park, J. Y.; Zhang, Y.; Grass, M.; Zhang, T.; Somorjai, G. A. *Nano Lett.* **2008**, *8*, 673−677.
(35) Porsgaard, S.; Ono, L. K.; Zeuthen, H.; Knudsen, J.; Schnadt, J.; Merte, L. R.; Chevallier, J.; Helveg, S.; Salmeron, M.; Wendt, S.; Besenbacher, F. *ChemPhysChem* **2013**, *14*, 1553−1557.
(36) Gao, F.; Wang, Y.; Cai, Y.; Goodman, D. W. *J. Phys. Chem. C* **2009**, *113*, 174−181.
(37) Knudsen, J.; Nilekar, A. U.; Vang, R. T.; Schnadt, J.; Kunkes, E. L.; Dumesic, J. A.; Mavrikakis, M.; Besenbacher, F. A. *J. Am. Chem. Soc.* **2007**, *129*, 6485−6490.

DOI: 10.1021/acscatal.6b02054
ACS Catal. 2017, 7, 191−204